Materials Science & Engineering A 953 (2026) 149705

Contents lists available at ScienceDirect

Materials Science & Engineering A

journal homepage: www.elsevier.com/locate/msea

In-situ investigation of the slip activities, deformation twinning, and cracking behavior of a bimodal Ti-6Al-3Nb-2Zr-1Mo alloy

Yafei Wang [a], Shuangjie Chu [a,b,*], Xing Zhang [c], Wanting Sun [d], Qifei Zhang [a,e], Qian Liu [a], Soban Muddassir Dar [a], Bohao Zhou [a], Jifeng Sun [e], Gaofei Liang [e], Haiyan Zhao [a,e], Bo Mao [a,**]

[a] School of Materials Science and Engineering, Shanghai Jiao Tong University, Shanghai, 200240, China
[b] Baoshan Iron & Steel Co., Ltd., Shanghai, 201900, China
[c] School of Mechanical and Electric Engineering, Soochow University, Suzhou, 215100, China
[d] School of Engineering, Lancaster University, Lancaster, LA1 4YW, UK
[e] Baowu Special Metallurgy Co., Ltd., Shanghai, 200940, China

ARTICLE INFO

Keywords:
Ti-6Al-3Nb-2Zr-1Mo (wt.%) alloy
In-situ EBSD analysis
Dislocation slip
Twinning deformation
Cracking behavior

ABSTRACT

In this study, the deformation mechanisms and damage evolution behavior in a bimodal Ti-6Al-3Nb-2Zr-1Mo (wt.%) alloy were systematically investigated via the combination of advanced in-situ EBSD analysis of tensile testing and transmission electron microscopy (TEM) observation. The slip trace analysis demonstrates that the early stage of plastic deformation is dominated by the prismatic <a> and basal slip systems, whereas the pyramidal <a> and <c+a> slip systems are gradually activated and become the primary deformation mechanisms at high strain levels. Specifically, the plastic deformation is mainly accommodated by the presence of α phase through the basal and the prismatic slip systems. Besides, the Schmid factors of the basal and prismatic slip systems under the given loading direction are significantly lower than that of the pyramidal slip system, and thereby the pyramidal slip is preferential activated during the plastic deformation. With increasing strain, the lamellar α phase progressively activates the pyramidal <c+a> slip systems to accommodate the imposed strain along the c-axis. TEM observations exhibit the presence of high-density dislocation tangles near twin boundaries, and thus the synergistic interaction between dislocation slip and twining can induce the micro-void nucleation and growth, which is driven by the localized stress concentration. This work elucidates the damage mechanisms dominated by the slip-twinning interactions, which can provide theoretical guidance for strength-ductility optimization in bimodal titanium alloys.

1. Introduction

Titanium (Ti) alloys with bimodal microstructures have garnered tremendous attention in aerospace, biomedical, and marine engineering fields due to their unique microstructural characteristics and the comprehensive mechanical properties caused by distinct deformation mechanisms [1–3]. In general, Ti alloys containing equiaxed α grains and lamellar α/β colonies usually possess the advantageous combination of strength and ductility together with exceptional fracture toughness, which make them suitable for extremely operational environments such as deep-sea pressure vessels and marine propulsion systems. Particularly, the bimodal Ti-6Al-3Nb-2Zr-1Mo (wt.%) (Ti-6321) alloy has emerged as a promising candidate for marine applications owing to its excellent environmental adaptability and mechanical performance [4–6]. Nevertheless, the understanding of the relationship between the bimodal microstructure and the underlying deformation mechanisms and damage tolerance are still required to be further explored, which is regarded as a knowledge gap that impedes microstructure-informed design for Ti alloys for service in extreme environments.

The mechanical behavior of bimodal Ti-6321 alloy is inherently dictated by the competition between slip systems and deformation twinning within its dual-phase structure constituents. Plastic deformation in hexagonal close-packed (HCP) α-Ti involves complex mechanisms, including basal, prismatic, and pyramidal slip systems, as well as

* Corresponding author. School of Materials Science and Engineering, Shanghai Jiao Tong University, Shanghai, 200240, China.
** Corresponding author.
E-mail addresses: sjchu@baosteel.com (S. Chu), bmao@sjtu.edu.cn (B. Mao).

https://doi.org/10.1016/j.msea.2025.149705
Received 3 July 2025; Received in revised form 21 November 2025; Accepted 29 December 2025
Available online 3 January 2026

deformation twinning [7–9]. The activation of these deformation mechanisms is primarily governed by crystallographic orientation, Schmid factors (SFs), and local stress states, which vary significantly between equiaxed and lamellar structures [10–12]. For example, in equiaxed α grains, the initial deformation stage is dominated by basal slip due to its lower critical resolved shear stress (CRSS) [12,13], which can promote homogeneous strain distribution. In contrast, the lamellar α/β colonies of Ti alloys are favorable for prismatic or pyramidal slip in HCP-α phase under the geometric constraints imposed by the β-phase, which restricts dislocation motion along the basal plane and facilitates the activation of non-basal slip systems [10,14]. When larger stress is imposed, the pyramidal slip with high CRSS can be activated and contribute to the strain accommodation of c-axis. Additionally, deformation twinning, especially $\{10\bar{1}2\}\langle\bar{1}011\rangle$ tensile twins, the mechanical behavior can be significantly affected by the formation of deformation twinning through reorienting grains to favor slip activation, which can also introduce localized stress concentrations that may accelerate the generation of damage. The above deformation mechanisms have been well elaborate in conventional commercial Ti alloys, such as Ti-6Al-4V (wt.%), but their precise interplay in bimodal Ti-6321 alloy remains insufficiently understood. Notably, the addition of Nb, Zr, and Mo elements [15–17] can affect the phase stability, interfacial cohesion, and CRSS ratios, which makes deformation dynamics become complex.

Beyond the microstructural constituent-specific deformation mechanisms, the interfaces between equiaxed grains and lamellar colonies, as well as the α/β phase boundaries within lamellar structures can serve as key sites for stress localization, dislocation accumulation, and twin nucleation, thereby governing damage evolution in bimodal Ti alloys. For instance, in conventional systems such as Ti-6Al-4V (wt.%), it was reported that slip bands preferentially nucleated at α/β lamellar interfaces and then propagated into equiaxed α grains, in which the slip activity was transited from single to multiple slip systems as the strain increased [18]. Similarly, in an earlier study, the microcrack initiation within TC21 alloy was mainly attributed to strain incompatibility between equiaxed grains and lamellar colonies [11]. Accordingly, in the case of Ti-6321 alloy, the presence of Nb, Zr, and Mo alloying elements is expected to influence interfacial slip transmission through solute–dislocation interactions and to mitigate strain localization by enhancing the β phase stability. However, the strain-dependent interplay between interfacial damage nucleation and cooperative plastic deformation across microstructural constituents remains insufficiently quantified. It is critical for marine applications, where cyclic loading promotes the initiation and propagation of microcracks at microstructural interfaces, thereby accelerating the damage.

To bridge these gaps, in the present study, advanced in-situ electron backscatter diffraction (EBSD) and transmission electron microscopy (TEM) techniques were employed to systematically explore the deformation mechanisms and damage evolution in bimodal Ti-6321 alloy under uniaxial tensile loading conditions. Specifically, the dynamic interactions among slip activities, deformation twinning, and micro-crack initiation were investigated, which can provide an in-depth understanding of how these mechanisms collectively influence microstructural evolution and mechanical performance of bimodal Ti-6321 alloy. This work aims not only to clarify the roles of different slip systems and twinning modes in dual-phase Ti alloy but also to quantify their relative contributions and interactions throughout progressive deformation stages. By revealing these complex interactions, the study intends to offer valuable insights into microstructural optimization strategies that could significantly enhance the mechanical properties of bimodal Ti-6321 alloy.

2. Materials and experiments

In this study, the raw material was a hot rolled Ti-6321 alloy sheet provided by Baowu special metallurgy Co., Ltd. To obtain a homogeneous and bimodal microstructure, the as-rolled samples were annealed at 980 °C for 4 h and subsequently air-cooled to room temperature.

The specimen for the in-situ tensile test was prepared via mechanical processing, with a total length of 70 mm and a thickness of 1 mm (Fig. 1c). Prior to testing, the sample surface was ground by abrasive paper followed by vibration polishing to achieve a high-quality surface finish for EBSD analysis. As shown in Fig. 1d, the tensile specimen was placed within a field emission scanning electron microscope (SEM, Sigma 500, Zeiss) equipped with a force-displacement sensor to perform a displacement-controlled in-situ tensile test. Specifically, the in-situ tensile test was conducted at a displacement rate of 2 μm/s, with interruptions at four critical strain points to enable in-situ EBSD characterization of the evolving microstructure. To examine the microstructure evolution, four interruption points were selected during the tensile test (Fig. 1a), corresponding to the key stages of stress-strain response (i.e., engineering strain of 1 %, 6 %, 11 %, 16 %) (Fig. 1b). EBSD analysis was performed with an acceleration voltage of 20 kV and a working distance of 10 mm. The scanning step size was set to 0.3 μm for macroscopic regions and 0.12 μm for local regions, respectively. The corresponding EBSD data were post-processed using the AZetcCrystal software. The slip trace analysis was performed using the custom-developed STrCry software (https://github.com/shaolouwei/STrCryst). Throughout the in-situ tensile test, SEM imaging, forescatter detector (FSD) imaging and EBSD scanning were systematically conducted on the gauge section of the specimen to monitor dynamic microstructure evolution upon loading.

After in-situ tensile testing, the deformed specimen was sectioned into 3-mm-diameter discs and mechanically polished to a thickness of approximately 50 μm. Thin foils for TEM observation were subsequently prepared via twin-jet electropolishing using a solution composed of perchloric acid, methanol, and butanol in a volume ratio of 6:64:30. The deformed bimodal microstructure of Ti-6321 alloy was then characterized using Talos F200X field-emission TEM (operating at 200 kV) to observe phase morphology, dislocation activity, and strain-induced microstructure evolution.

3. Results

3.1. Initial microstructure

Fig. 2 presents the initial microstructure of the Ti-6321 alloy after annealing process. As shown in Fig. 2a, the microstructure exhibits a typical bimodal structure, which is composed of equiaxed α-phase grains and lamellar α+β colonies (transformed from the prior β matrix). Fig. 2b displays the inverse pole figure (IPF) map of the same region, where grain boundaries with misorientations between 2° and 15° are classified as low angle grain boundaries (LAGBs), while those exceeding 15° are defined as high angle grain boundaries (HAGBs). The phase distribution map (Fig. 2c) reveals the spatial arrangement of the α phase (red) and β phase (green). It can be found that β phase is uniformly distributed within the matrix accounting for only 1.7 vol%. TEM observation further reveals the bimodal microstructure, highlighting the coexistence of equiaxed α-phase grains and β-transformed lamellar colonies, as shown in Fig. 2d. The EDS elemental mapping clearly elucidates the composition partitioning between the α and β phases. Aluminum (Al), a well-known α-Ti stabilizer, is uniformly distributed within the α phase, with slightly lower concentrations observed in the β phase. Conversely, molybdenum (Mo) and niobium (Nb), as β-Ti stabilizers, exhibit limited solubility in the α phase but are significantly enriched in the β phase. Zirconium (Zr), as a neutral element in Ti alloys, displays a homogeneous distribution across the matrix without any preferential solute segregation to either phase.

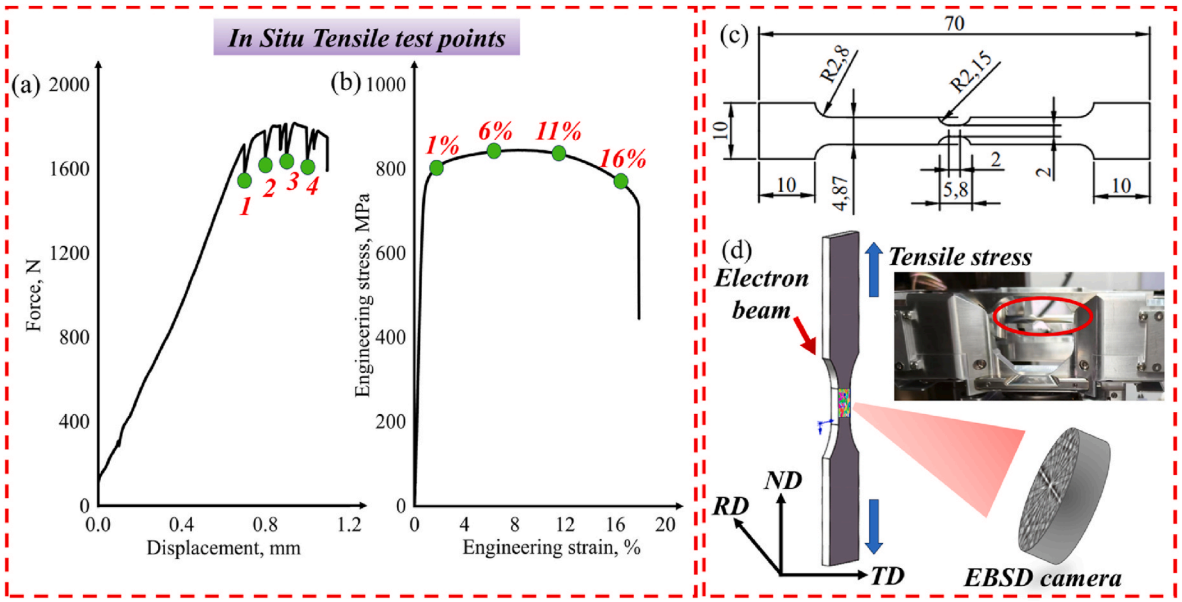

Fig. 1. (a) Force-displacement curve (Points 1, 2, 3 and 4 correspond to the in-situ EBSD characterization points, respectively.) and (b) engineering stress-strain curve (The four interrupt points correspond to the engineering strain of 1 % (Point 1), 6 % (Point 2), 11 % (Point 3) and 16 % (Point 4)) of the Ti-6321 alloy during in-situ tensile tests. (c) Schematic diagram of in-situ tensile sample size. (d) Schematic diagram of the in-situ EBSD test and illustration of the in-situ tensile device (red circle indicates the in-situ tensile specimen). (For interpretation of the references to colour in this figure legend, the reader is referred to the Web version of this article.)

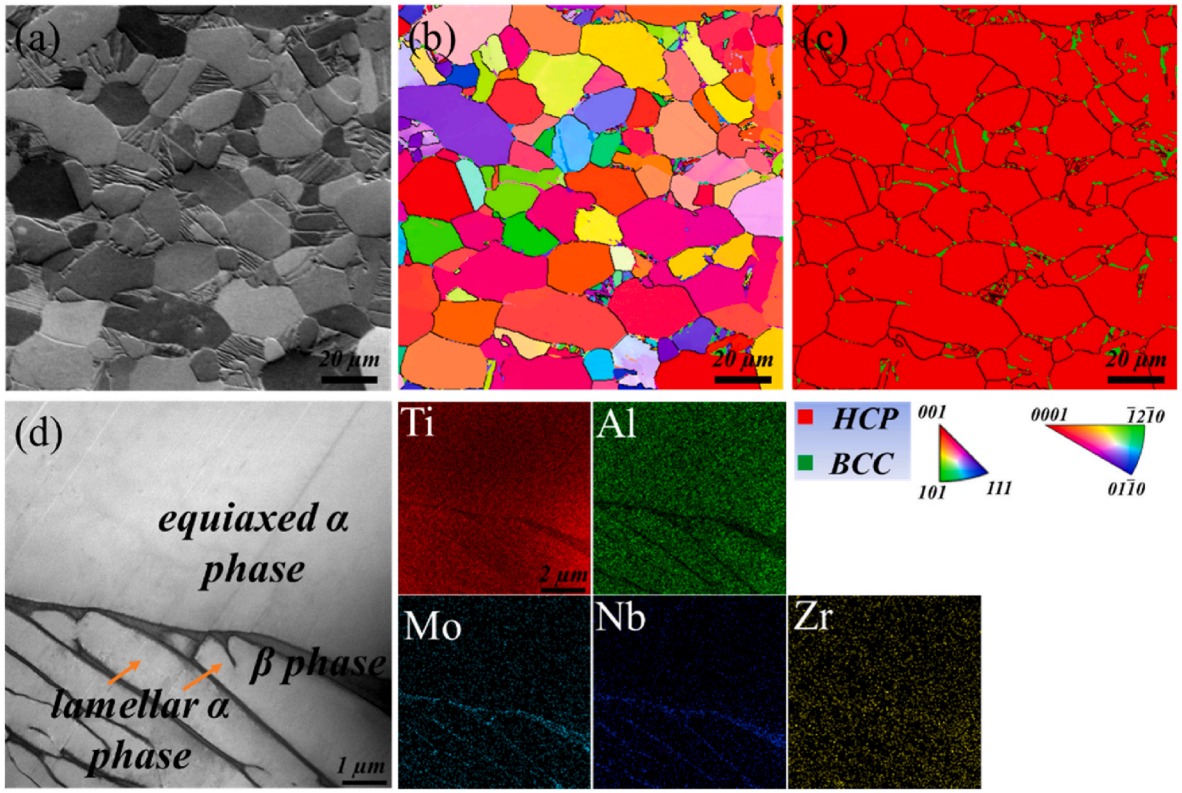

Fig. 2. Microstructure of the as-received Ti6321 alloy: (a) FSD image, (b) IPF map and (c) phase distribution map (red: HCP α-phase; green: BCC β-phase). (d) TEM image of equiaxed α-phase, lamellar α+β colonies in Ti-6321 alloy, along with the corresponding EDS mapping results showing the distribution of different alloy elements. (For interpretation of the references to colour in this figure legend, the reader is referred to the Web version of this article.)

3.2. Slip trace and dislocation activation

Fig. 3 shows the in-situ EBSD-SEM analysis of the microstructure evolution of Ti-6321 alloy with progressive deformation process. The development of surface slip traces is essentially caused by the directional movement of dislocations along specific slip systems [18]. Fig. 3d–f exhibit the strain-dependent microstructure evolution, revealing macrozone morphological transitions in the Ti-6321 alloy during the plastic

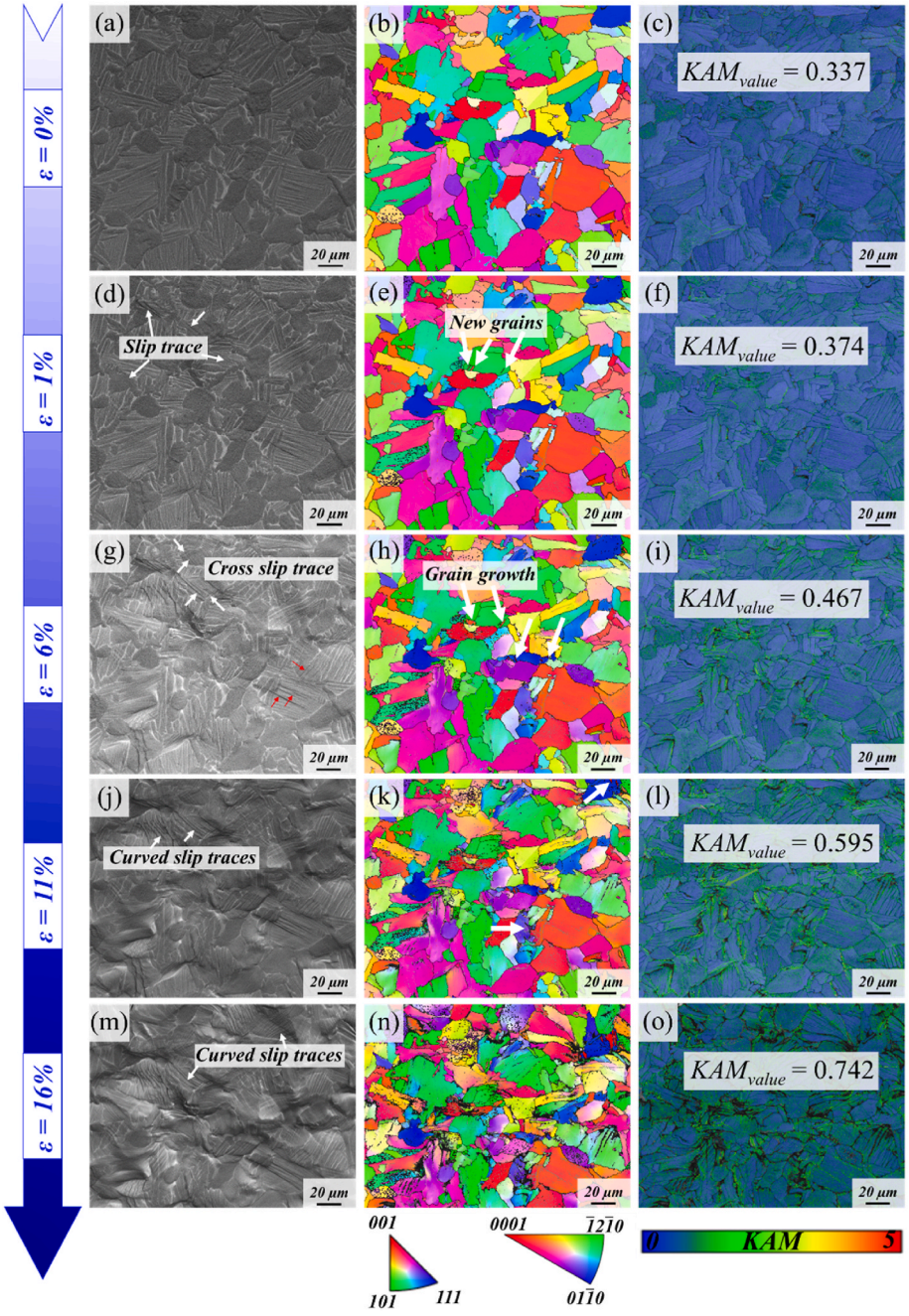

Fig. 3. In-situ SEM and EBSD analysis of the microstructure evolution of Ti-6321 alloy: (a, d, g, j, m) SEM images, (b, e, h, k, n) IPF maps, (c, f, i, l, o) KAM + BC maps and KAM distributions of the samples deformed at strain levels of 0 %, 1 %, 6 %, 11 % and 16 %.

deformation. Compared with the SEM images of the initial macrozone (Fig. 3a), it is evident that the activation behavior of the slip traces and slip systems in Ti-6321 alloy exhibits dynamic characteristics with increasing strain. As shown in Fig. 3d (strain of 1 %), straight and uniformly spaced slip traces are observed in equiaxed α grains, with similar features appearing in some lamellar colonies. These traces at an early stage of deformation indicate the initiation of dislocation glide. In contrast, as 6 % strain (Fig. 3g), bifurcated and intersecting traces appear, implying the activation of multiple slip systems. Generally, the slip traces in equiaxed α grains terminate at grain or phase boundaries, while in the lamellar colonies they can cross interfaces and propagate into adjacent lamellar structures (highlighted by red arrows in Fig. 3g). As the strain increases to 11 % (Figs. 3j) and 16 % (Fig. 3m), it can be found that the slip traces become curved, which is possibly attributed to grain rotation that alters the relative orientation between slip systems and the tensile loading axis.

The kernel average misorientation (KAM) distribution maps obtained from EBSD data reflect the accumulation of geometrically necessary dislocations (GNDs). Initially, the KAM values are relatively low and exhibit uniformly distribution (0.3°–0.5°). As strain increases, the increased KAM values in lamellar α phase demonstrate the enhanced dislocation activity through multi-slip and cross-slip mechanisms, which efficiently accommodate plastic strain. Quantitative KAM analysis reveals that the mean misorientation angles systematically increase from 0.337 (undeformed state) to 0.374 ($\varepsilon = 1$ %), 0.467 ($\varepsilon = 6$ %), 0.595 ($\varepsilon = 11$ %), and 0.742 ($\varepsilon = 16$ %), respectively. This monotonic rise in KAM values provides direct evidence for the continuous accumulation of GNDs during the plastic deformation [18], which also implies the

enhancement of dislocation entanglement and dislocation interaction. To exclude the influence of twinning, another deformation mode in HCP metals, we excluded grains containing common twins from the analysis of both the IPF maps and the KAM/BC maps [19]. This approach allows for a more accurate confirmation that the increase in average misorientation with strain is attributable to dislocation activity and slip-dominated plasticity. The detailed post-processed images are presented in Supplementary Fig. S1. This crucial methodological step allows us to state with high confidence that the observed misorientation evolution in this analyzed grain population is primarily attributable to the accumulation of geometrically necessary dislocations (GNDs) from slip activity. To further analyze slip system activation, theoretical slip traces and SFs were calculated using Euler angles via MATLAB [20] and subsequently correlated with experimentally observed slip traces. It should be noted that for Ti alloys, the main slip modes of the HCP α phase include the <a> type basal slip system $\{0001\}\langle 11\bar{2}0\rangle$ [21], the prismatic slip system $\{10\bar{1}0\}\langle 11\bar{2}0\rangle$ [22], the 1st-order pyramidal slip system $\{10\bar{1}1\}\langle 11\bar{2}3\rangle$ [9], and 2nd-order pyramidal slip system $\{11\bar{2}2\}\langle 11\bar{2}3\rangle$ [23]. In this study, when multiple theoretical slip systems correspond to an observed slip trace, the slip system with the highest SF can be assumed to be activated [11,18].

Fig. 4a presents the IPF map of microregions, where the microstructure is partitioned into 30 distinct grains (designated as G_1 through G_{30}) based on HAGBs (>15°). Fig. 4b displays the corresponding FSD + GB map of the microregions. Fig. 4c–j exhibit IPF maps and FSD + grain boundary (GB) maps at strain of 1 %, 6 %, 11 % and 16 %, respectively. It can be found that at a strain of 1 %, discernible slip traces are identified in 14 out of 30 grains, corresponding to the activation of 19 distinct slip traces. The distributions of these slip traces can be described by the following order: basal <a> (26.3 %), prismatic <a> (31.6 %), pyramidal <a> (26.3 %) and pyramidal <c+a> (15.8 %). Such distributions indicate that basal and prismatic slip systems, which generally possess lower CRSS, are preferentially activated in the early stages of deformation. However, when the loading direction favors a higher SF for pyramidal systems, these higher-CRSS slip systems may be activated instead. This behavior reflects the influence of crystallographic characteristics and SF distribution on slip system selection. As strain increases to 6 %, 11 %, and 16 % (Fig. 4f, h, and 4j), the proportions of slip traces (marked by red and green traces, respectively), representing 1st-order and 2nd-order pyramidal slip systems, significantly increases. This trend indicates progressive activation of pyramidal slip systems under elevated stress and continuous grain reorientation during plastic deformation.

Although prismatic and basal slip systems are generally considered to be the primary deformation modes at low strains, the observed slip traces also include pyramidal systems. This discrepancy can be attributed to the orientation-dependent SFs. Specifically, in some certain grains, the SF for basal slip could be lower than that of pyramidal slip, making the latter energetically more favorable despite its higher CRSS. To evaluate the preferential activation of slip systems under the applied loading direction, the SFs of each system were calculated based on the Euler angles obtained from EBSD data.

During tensile deformation, grain rotation may occur which alters the angle between slip planes and the loading axis, and thereby the SF values are changed that affect the sequence of slip system activation. Fig. 5 shows the calculated SF values for each theoretical slip traces in each grain. At 1 % strain, the SFs of 4 out of 5 activated basal slip traces, 3 out of 6 activated prismatic slip traces, and 3 out of 5 activated 1st-order pyramidal slip traces exceed 0.3. Although fewer in number, 2nd-order pyramidal systems show SFs consistently greater than 0.25. With increasing strain, the activation of pyramidal systems becomes more prevalent: at 6 % strain, the SFs of 10 out of 12 activated 1st-order pyramidal slip traces and 6 out of 8 activated 2nd-order pyramidal slip traces exceed 0.3. This proportion increases further at 11 % strain (10/12 and 8/9, respectively), and remains high at 16 % strain (9/10 and 6/7, respectively). These results underscore the important role of grain reorientation in governing slip system activity. Initially dominant systems are progressively replaced by the slip systems with increasingly favorable SFs, highlighting a competitive multi-slip behavior as the plastic deformation proceeds.

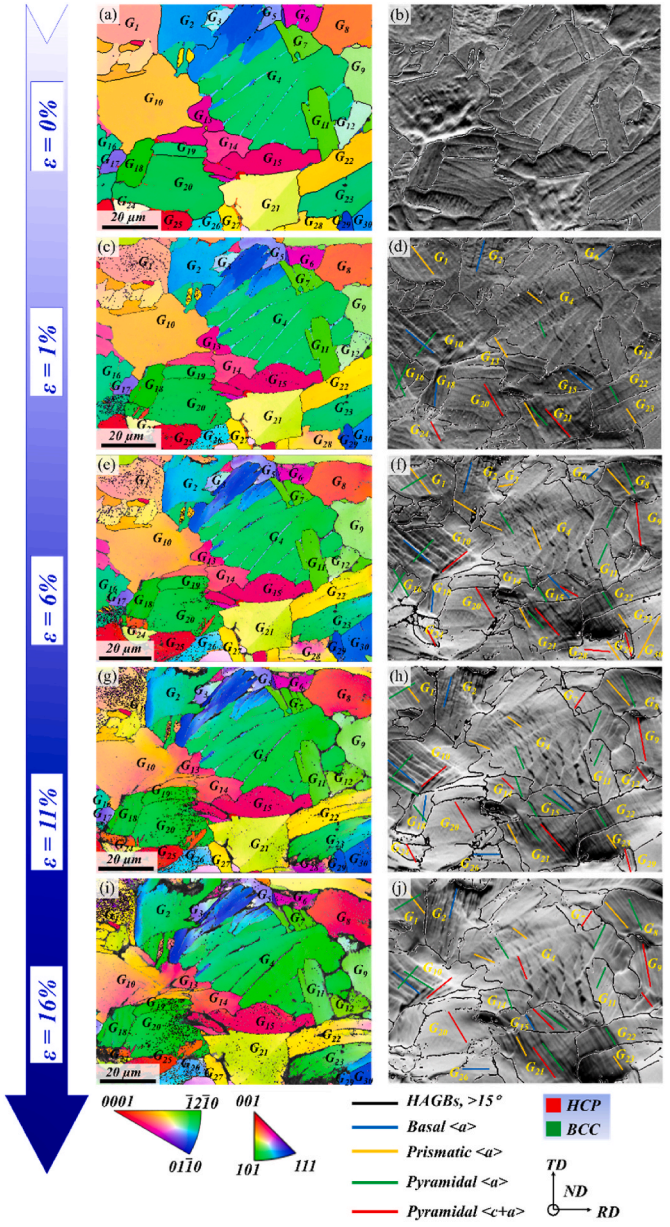

Fig. 4. IPF maps at strain of (a) 0, (c) 1 %, (e) 6 %, (g) 11 % and (i) 16 %. (Individual grains in this area are labeled as G1~G30, respectively). FSD + GB maps at strains of (b) 0 %, (d) 1 %, (f) 6 %, (h) 11 %, and (j) 16 %. (The blue lines represent basal slip system, orange lines indicate prismatic slip system, the green lines are 1st-order pyramidal slip system, and the red lines demonstrate the 2nd-order pyramidal slip system.). (For interpretation of the references to colour in this figure legend, the reader is referred to the Web version of this article.)

3.3. *Initiation and development of* $\{10\bar{1}2\}\langle\bar{1}011\rangle$ *twins*

Due to the limited slip systems in HCP α phase, dislocation slip alone is often insufficient to accommodate the plastic strain during tensile deformation. Accordingly, deformation twinning may appear as a complementary deformation mechanism, especially under conditions

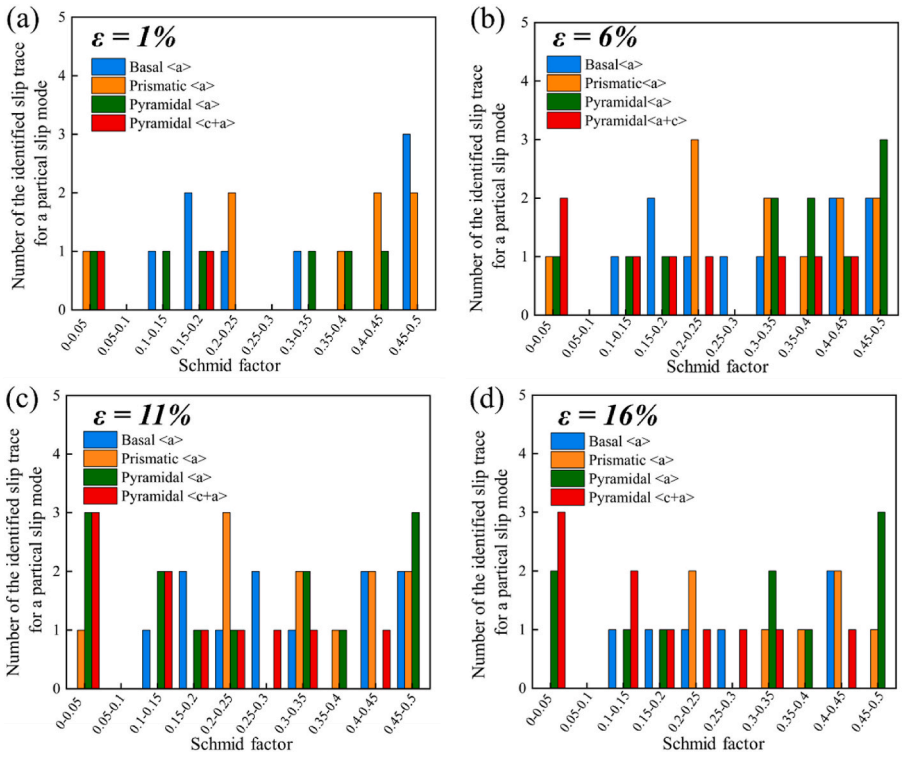

Fig. 5. Distributions of Schmid factor (SF) values for the identified slip systems under the imposed strains of (a) 1 %, (b) 6 %, (c) 11 %, and (d) 16 %.

where additional strain accommodation is required [24]. As presented in Fig. 4, the nucleation and growth of new grains can be observed within the β transformed structure G_{20} as the strain increases. Misorientation analysis between the parent grain and newly formed grains

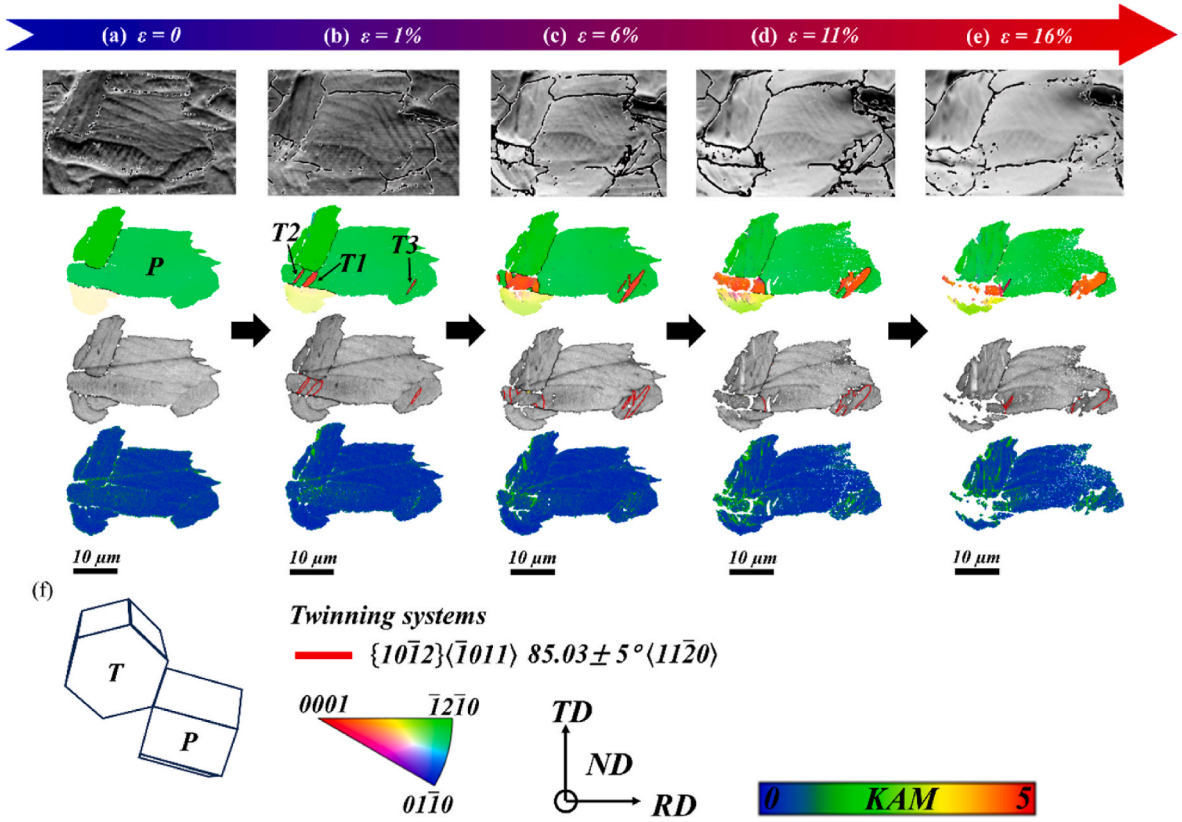

Fig. 6. (a) Local IPF map of the parent grain. Local IPF maps at strains of (b) 1 %, (c) 6 %, (d) 11 %, (e) 16 %, respectively. (f) Orientation relationship between the parent grain and its twin.

reveals a misorientation angle of approximately 87°, suggesting that these features can be identified as deformation twin [25]. Additionally, to verify the specific twinning mode, a comparative analysis of FSD images, local IPF maps, BC maps, and KAM distributions for grain G_{20} at different strain levels were conducted (Fig. 6). By labeling six common twin variants in the BC maps, the newly formed grains can be identified as $\{10\bar{1}2\}\langle\bar{1}011\rangle$ tensile twins. As shown in Fig. 6b, the twin initially nucleates and grows along a specific crystallographic plane. However, at higher strain levels (6 % in Figs. 6c and 11 % in Fig. 6d), the twin growth is impeded upon encountering grain boundaries or phase interfaces. These high-energy interfaces act as effective barriers to twin propagation, leading to a redirection of growth into alternative crystallographic orientations [26]. This redirection ultimately results in lateral expansion of the twin [27]. KAM maps further reveal that the formation of deformation twins is associated with localized accumulation of GNDs near twin boundaries that reflected by the increased misorientation values. Besides, the abrupt lattice misorientation acts as a barrier to dislocation motion, leading to the dislocation pile-ups and localized stress concentrations.

The $\{10\bar{1}2\}\langle\bar{1}011\rangle$ tensile twinning mode in Ti alloy can induce shear deformation that reorients the c-axis of HCP α phase, and thus the c-axis is transformed from an initially unfavorable orientation for slip into the one that can promote subsequent plastic deformation [28]. Such lattice reorientation can compensate for the lack of available slip systems in HCP structures, and thereby the plastic strain accommodation is facilitated. Based on the TEM observation as shown in Fig. 7a demonstrates significant dislocation pile-ups near the twin boundaries. These dislocation pile-ups are derived from the obstruction of matrix dislocation motion by high-energy twin boundaries that serve as strong barriers, leading to the formation of high-density dislocation zones [20,29]. A high-resolution TEM (HR-TEM) image (Fig. 7b) clearly displays the mirror symmetry between matrix and twin regions across the interface. The corresponding fast Fourier transform (FFT) analysis confirms an 86° misorientation between the twin and the matrix, with both sharing a common $[1\bar{2}10]$ zone axis orientation, which is consistent with the crystallographic relationship of $\{10\bar{1}2\}\langle10\bar{1}1\rangle$ deformation twins in HCP metals. Eventually, this specific orientational symmetry results in the typical mirror-symmetric structure observed at the twin boundary [29].

4. Discussion

To investigate the micromechanical evolution mechanism of equiaxed α grain (G_{10}) and lamellar-structured grain (G_4) in the Ti-6321 alloy during in-situ tension, systematic analyses of slip trace were conducted for each microstructural region.

4.1. Slip traces and dislocation motion in equiaxed α phase

Fig. 8 presents a comparative analysis between the experimentally observed dislocation slip traces activated in equiaxed α grain (G_{10}) under varying strain conditions and their corresponding theoretical predictions on the basis of crystallographic slip modes. At low strain levels, basal slip $\{0001\}\langle11\bar{2}0\rangle$ with lower CRSS in the equiaxed α grain is preferentially activated. Dislocations glide over long distances along individual slip planes, and the straight and continuous slip traces are generated (Fig. 8a). Furthermore, the SFs for pyramidal slip system $\{\bar{1}011\}\langle\bar{1}2\bar{1}0\rangle$ is approximately 0.5 under these conditions, indicative of a favorable stress orientation. The dislocation motion is facilitated by the high resolved shear stress, and thus the linear slip traces are formed. As 6 % strain, the activation of additional pyramidal slip system $\{2\bar{1}\bar{1}2\}\langle2\bar{1}\bar{1}\bar{3}\rangle$ introduces the intersection and deflection of slip traces due to differing slip directions (Fig. 8b). As the strain increases to 11 % and 16 %, grain rotation can change the crystallographic orientation relative to the applied load, and the SFs for the previously suboptimal slip system such as $\{01\bar{1}1\}\langle2\bar{1}\bar{1}0\rangle$ are increased, suggesting that the grain reorientation promotes the activation of multiple slip systems to form complex slip traces.

To further investigate the dislocation evolution characteristics and slip system activation behavior of the equiaxed α grains in Ti-6321 alloy during the plastic deformation, TEM characterization was performed. Fig. 9a displays bright-field TEM image and the corresponding SAED patterns of the equiaxed α grain extracted from the in-situ tensile specimen. The magnified region (yellow rectangular region) in Fig. 9b reveals parallel dislocation lines are preferentially aligned along a specific crystallographic direction, along with localized accumulation of highly entangled dislocation networks. These microstructure configurations are consistent with the activation of basal <a> slip $\{0001\}\langle11\bar{2}0\rangle$ or prismatic <a> slip $\{1\bar{1}00\}\langle11\bar{2}0\rangle$ systems at the early stage of deformation, which serve as a dominated deformation mode in the α grains with specific crystallographic orientation relative to the applied load.

When the resolved shear stress acting on these slip systems reaches the CRSS parallel dislocations nucleate and glide toward grain boundaries, where the dislocation motion is impeded, leading to the formation of dislocation pile-ups near the grain boundaries [30,31]. With increasing strain, secondary slip systems such as pyramidal <a> and pyramidal <c+a> slip are gradually activated, and the interaction of the primary slip system can be detected. This multi-slip interaction leads to the localized accumulation of dislocations,and thereby the localized

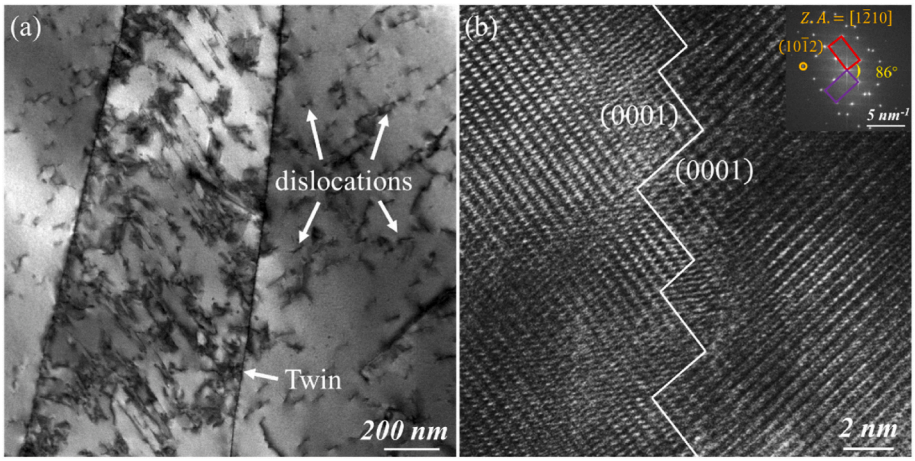

Fig. 7. (a) TEM image showing deformation twins formed under tensile loading. (b) HR-TEM image of a typical $\{10\bar{1}2\}\langle10\bar{1}1\rangle$ tensile twin and the corresponding FFT pattern.

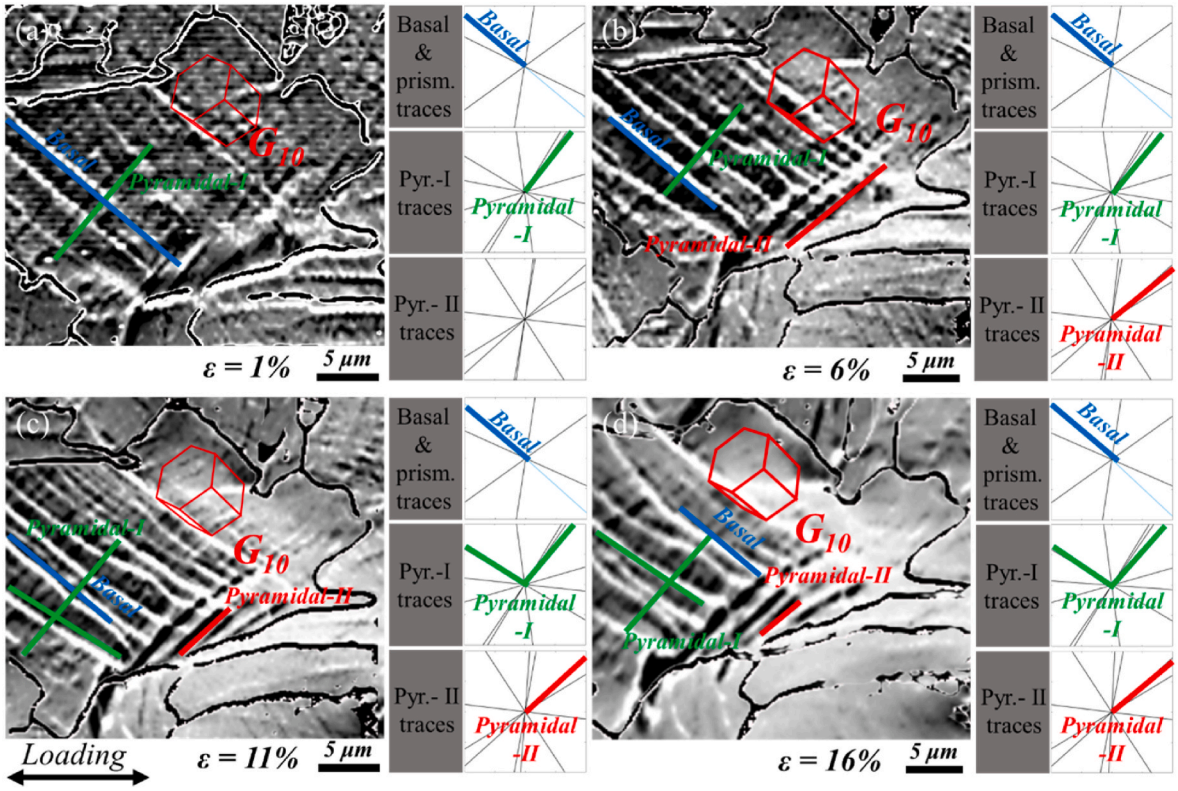

Fig. 8. FSD images + GB maps of equiaxed grain G_{10} at engineering strain of (a) 1 %, (b) 6 %, (c) 11 % and (d) 16 %. (Basal & prismatic traces represent theoretical basal <a> slip trace and prismatic <a> slip traces, Pyr. - I traces represent theoretical pyramidal <a> slip traces, Pyr. - II traces represent theoretical pyramidal <c+a> slip traces).

high-density dislocation tangles are formed [32]. As shown in Fig. 9c and e, dislocation characteristics were further examined using contrast analysis under two imaging conditions, with distinct beam diffraction vectors parallel to the {0002} and $\{10\bar{1}0\}$ orientations, respectively. Under the diffraction condition of {0002} basal plane vector (Fig. 9d), the linear dislocations exhibit contrast extinction which can be identified as <a> type dislocations with Burger vector $\mathbf{b} = 1/3\langle 11\bar{2}0\rangle$. These dislocations are preferentially activated in low-strain regions and contribute significantly to plastic accommodation. As <a> type dislocations are accumulated at grain boundaries, leading to significant dislocation pile-ups. In contrast, under the $\{10\bar{1}0\}$ prismatic plane diffraction condition (Fig. 9f), the high-density dislocation tangles can be observed. Based on the Burgers vector analysis, it is conclusively determined that these entangled dislocations are assigned to <c> type dislocations. Due to their relatively high resolved shear stress and limited cross-slip ability, these dislocations nucleate within some specific regions, but they play an essential role in accommodating strain along the c-axis of HCP structure.

4.2. Slip traces and dislocation motion in β transformed structure

Fig. 10 presents the comparative analysis between the experimentally observed and theoretically predicted slip traces in the lamellar-structured grains (G_4) under different strain levels. At the strain of 1 % (Fig. 10a), both the prismatic and pyramidal <a> slip systems are activated. This co-activation could be attributed to the relatively low CRSS of prismatic slip system $\{10\bar{1}0\}\langle\bar{1}2\bar{1}0\rangle$ in the lamellar α-phase, which promotes homogeneous plastic deformation during the initial deformation stage. Meanwhile, the presence of α/β phase boundaries serve as significant obstacles to dislocation mobility, resulting in localized stress concentration. Once the accumulated stress surpasses the CRSS threshold for pyramidal <a> slip $\{01\bar{1}1\}\langle 2\bar{1}\bar{1}0\rangle$, the activation of secondary slip system occurs. As the strain progressively increases to 6 % (Figs. 10b) and 11 % (Fig. 10c), the grain rotation leads to the selective activation of prismatic slip systems with relatively low SFs. Concurrently, the pyramidal <a> slip systems are activated through synergistic interactions across multiple slip planes and slip directions. This complementary mechanism governed by prismatic slip can effectively alleviate the stress concentration accumulated at α/β phase interfaces during plastic deformation [33]. However, when the strain further increases to 16 % (Fig. 10d), significant deformation accumulation necessitates additional strain accommodation along the c-axis of HCP. Consequently, <c+a> slip pyramidal slip systems become operative once local resolved shear stress exceeds their CRSS, highlighting their crucial role in sustaining deformation at elevated strain levels under the tensile loading condition.

Fig. 11a displays the bright-field TEM image of the lamellar-structured grain and the corresponding SAED patterns of α phase from the in-situ tensile specimen acquired along the $[11\bar{2}0]$ zone axis. A magnified view of the yellow-marked area (Fig. 11b) reveals numerous intersecting dislocation lines with varying orientations within the lamellar α phase, indicating a more complex slip behavior compared to the equiaxed α phase, where the dislocations tend to align along some specific directions. Notably, high-density dislocation entanglement is absent in the lamellar α phase, indicating that the dislocations generated within the α phase may tend to either glide into the α/β interface or transform into interface dislocations at the α/β boundary [34]. Additionally, due to the greater number of active slip systems in the β phase, local stress concentrations within the lamellar α region are more effectively relieved, and thus extensive dislocation multiplication is diminished. This structural synergy between lamellar α phase and adjacent β phase promotes enhanced stress redistribution and contributes to the deformation stability.

To systematically analyze the dislocation characteristics in lamellar α

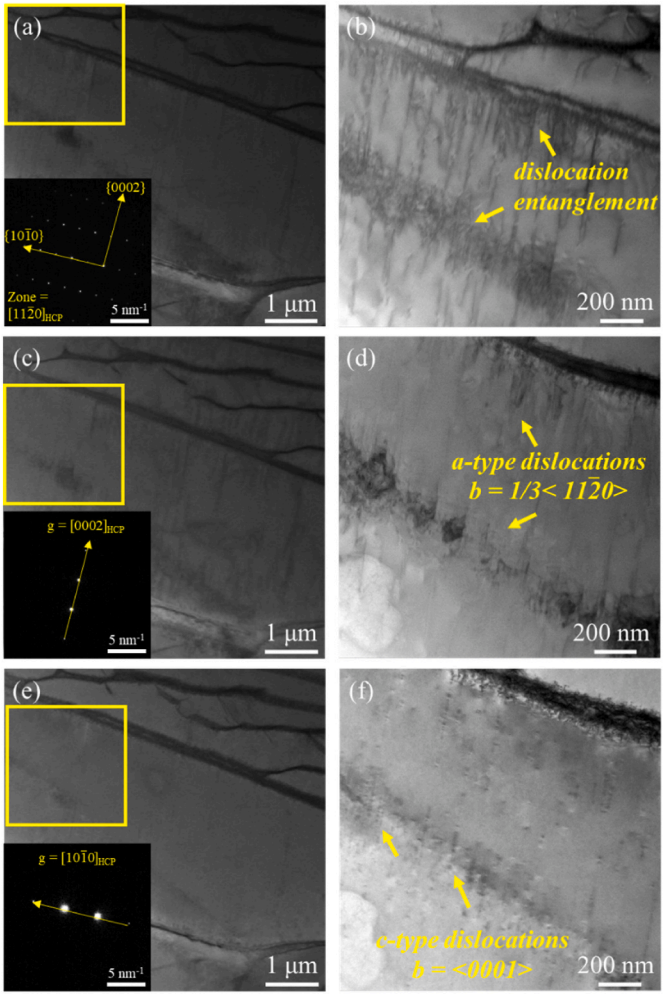

Fig. 9. (a) Bright-field TEM image of equiaxed structure and SAED pattern along [11$\bar{2}$0] zone axis. (b) High-magnification TEM image showing dislocation distribution along the [11$\bar{2}$0] zone axis. (c) Bright-field TEM image of equiaxed structure and SAED pattern of {0002} orientation. (d) High-magnification TEM image showing dislocation distribution along {0002} orientation. (h) Bright-field TEM image of the equiaxed structure and SAED pattern of {10$\bar{1}$0} orientation. (i) High-magnification TEM image showing dislocation distribution under {10$\bar{1}$0} orientation.

colonies, the dislocation morphologies were observed and analyzed in the {0002} and {10$\bar{1}$0} vectors. As shown in Fig. 11c, under the condition of {0002} basal vector, the partially dislocation line inside the lamellar α colonies presents an invisible phenomenon. As presented in Fig. 11d, these previously invisible dislocation lines are identified as <a> type dislocations with **b** = 1/3⟨11$\bar{2}$0⟩. As shown in Fig. 11d, the residual dislocation lines still exhibit visible contrast under this imaging condition. Further observation along the {10$\bar{1}$0} vector of lamellar α colonies reveals complete invisible of the dislocation contrast when the diffraction condition is transformed into the {0002} basal vector condition (Fig. 11e and f). Based on Burgers vector analysis and dislocation contrast invisible criteria, these dislocations can be determined as <c> type dislocations with Burger vector **b** = ⟨0001⟩. However, compared with the dense dislocation entanglement structure in the equiaxed α grain, the lamellar α colonies exhibit a relatively low density of <a> type dislocations, and the extensive <c> type dislocations can be also observed. This phenomenon might be ascribed to the predominant crystallographic orientation of the lamellar α colonies, in which the c-axis o is aligned parallel to the loading direction, and thus the SFs for the sliding systems including the basal <a> and the prismatic <a> are significantly reduced. Only a few <a> type dislocations are sporadically activated in the lamellae with specific orientations, and the dislocation movement is limited by the α/β phase interface, which hinders the formation of dense dislocation entanglements. Besides, the pyramidal <c+a> slip systems characterized by the high CRSS exhibit limited dislocation slip, and thus is rarely observed in the lamellar α colonies (Fig. 11f). When the dislocation movement is hindered due to the lamellae structure, preferred crystallographic orientation and interface characteristics of the lamellar α colonies, the deformation energy can be favorable for alternative deformation mechanism, i.e., twinning mode, which can effectively coordinate the strain on the c-axis of HCP structure in Ti alloy.

4.3. The initiation and propagation of micro-cracks

During the in-situ tensile deformation process, the surface of Ti-6321 alloy exhibits the tendency for crack initiation and propagation. Fig. 12a–d shows the SEM images of the sample surface at the strains of 1 %, 6 %, 11 % and 16 %, respectively. Compared with the microstructure as shown in Fig. 12a, the cracks become more pronounced with the increase of strain. EBSD analysis was conducted on this area at each strain, respectively. It can be found that surface cracks occur in the vicinity of deformation twins and then propagate along the LAGBs and HAGBs (Fig. 12g and h). For instance, micro-crack propagates along the slip trace through GB_3 (between P_2 and P_3), which exhibits a misorientation of 87.8°. Moreover, micro-cracks are also observed along GB_2 (between P_1 and P_3), GB_4 (between P_3 and P_4) which exhibits a misorientation of 64.5° and 61.7°. Based on the SEM images (Fig. 12c and d) and the IPF maps (Fig. 12g and h), it can be found that the deformation twins T_1 and T_2 association with the parent grains P_3 and P_5, respectively are formed along the micro-crack propagating along GB_3 and GB_4, suggesting that the twin boundaries act as preferential sites for crack nucleation and facilitate crack propagation, likely due to the localized stress concentrations and strain incompatibilities at twin boundaries. Under sustained mechanical loading, the orientation mismatch between the twin and the parent matrix leads to the activation of divergent slip systems and distinct strain responses [35,36]. To maintain strain continuity across the interface, significant local stress concentrations develop at the twin boundaries. This localized stress elevation may surpass the cohesive strength of the interface or the local fracture strength of the material, even in the absence of other microstructural defects, thereby acting as a potent precursor for crack initiation. Diiorio et al. [37] first observed that the twin boundaries were crack nucleation sites and special twins formed at 20 K led to the nucleation of cracks by a twin plane debonding process. Zhang et al. [38] studied the cracks by a dislocation-based crystal plasticity model and found the cracks always propagate near twins. Shen et al. [39] studied the stored energy density near HAGBs and found that higher stored energy for crack nucleation was accumulated near twin boundaries.

In previous studies, it demonstrated that the ductility of polycrystalline HCP materials can be affected by the local strain variations in adjacent grains [35]. In this case, during the in-situ tensile process of Ti alloy samples along the rolling direction, the plastic deformation of the sample surface is mainly accommodated by dislocation slips due to the low activities or limited growth capability of the twining system (Fig. 6). The activation of a specific slip system in individual grains can be determined by the Schmid law, which is dependent on the resolved shear stress acting along specific crystallographic slip directions and planes. Therefore, each grain might exhibit different degree of local plastic deformation, which is manifested by the slip traces produced by different grains (Fig. 4). Accordingly, it is essential to ensure the slip transfer across grain boundaries to maintain the deformation compatibility of Ti alloys during in-situ tensile process [40]. The deformation compatibility among adjacent grains can be evaluated by the geometric compatibility factor (GCF) proposed by Luster and Morris [41]. The

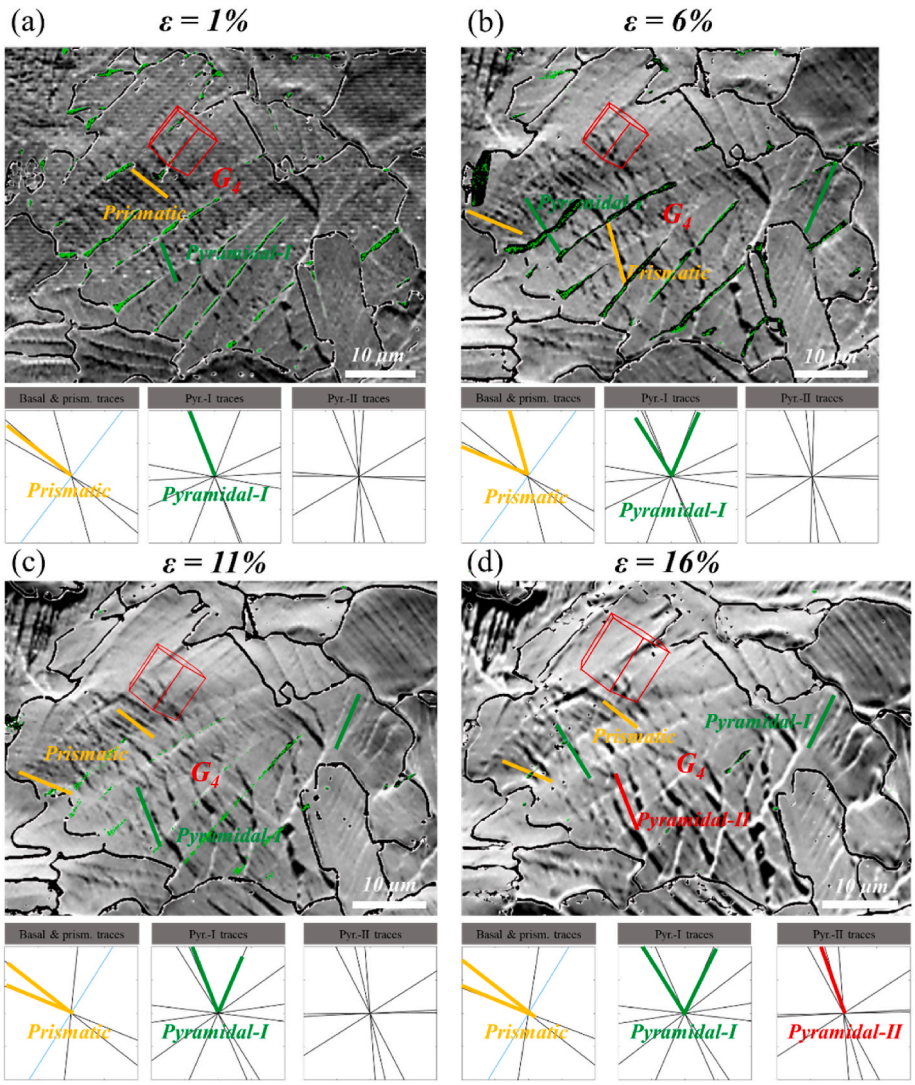

Fig. 10. FSD + GB + phase maps of lamellar-structured G4 at engineering strain of (a) 1 %, (b) 6 %, (c) 11 % and (d) 16 % (Basal & prism. traces represent theoretical basal <a> slip trace and prismatic <a> slip traces, Pyr. - I traces represent theoretical pyramidal <a> slip traces, Pyr. - II traces represent theoretical pyramidal <c+a> slip traces).

GCF, m', is defined as: $m' = cos\,\varphi \cdot cosk$, where the φ and k represent the angles between the slip directions and normal to the slip planes of the two adjacent grains, respectively. A high GCF indicates favorable geometric alignment of slip systems across the grain boundary, suggesting that the atomic arrangements at the boundaries are well-matched and exhibit an ordered configuration. Such coherent grain boundaries possess low interfacial energy, which can effectively impede the microcrack propagation, and then the fracture resistance of material can be enhanced.

Conversely, the incoherent interfaces corresponding to grain boundaries with a low GCF have obvious structural disorder characteristics. Firstly, their atomic arrangement shows obvious disorder characteristics. Besides, this random grain boundary often serves as preferential sites for the location of stress concentration, which facilitates the nucleation of micro-cracks during the deformation process. Therefore, such boundaries act as a low-resistance pathway for subsequent crack propagation to compromise the mechanical integrity of Ti alloy. In this study, the values of basal slip systems between P_1 and P_2, P_1 and P_3, P_2 and P_3, P_3 and P_4, P_3 and P_5, and P_4 and P_5, were calculated (Tables S1–6 in the supplementary information). It is apparent that the highest m' value between P_1 and P_2 is 0.8597, whereas it is 0.8295 between P_3 and P_5, indicating that GB_1 and GB_6 exhibit a superior strain compatibility without micro-cracks. Similarly, the highest m' value between P_1 and P_3, P_3 and P_4, and P_4 and P_5 are 0.4595 (Table 2S), 0.4634 (Table 4S), and 0.3955 (Table 6S), which is also higher than that between P_2 and P_3. The low GCF between P2 and P3 also confirms the generation and propagation of micro-cracks (Fig. 12). Furthermore, Ti alloys with bimodal microstructure are widely observed with the formation of $\{10\bar{1}2\}\langle\bar{1}011\rangle$ tensile twins during in-situ tensile. The formation of $\{10\bar{1}2\}\langle\bar{1}011\rangle$ tensile twins is driven by lattice shearing, which induces significant lattice distortion and localized high shear strain within the twin tip region [28]. This leads to pronounced stress concentration that affect the mechanical response within this region [42]. For HCP structure alloys, including Ti alloys, local high stress concentration around grain or twin boundaries can usually be alleviated by dislocation slip, twinning, or micro-crack nucleation during the plastic deformation [43,44].

As reported, the formation of microcracks at the twin boundaries was determined by the slip-twin boundary interaction [41], and the activated slip systems and twin types can affect whether the dislocations were accumulated or transmitted across the boundaries. It implied that the initiation of micro-cracks at the twin boundary was closely related to the difference in the SF of the activated dislocations between the matrix and the twin. As descripted in Fig. 12, it can be found that the interaction

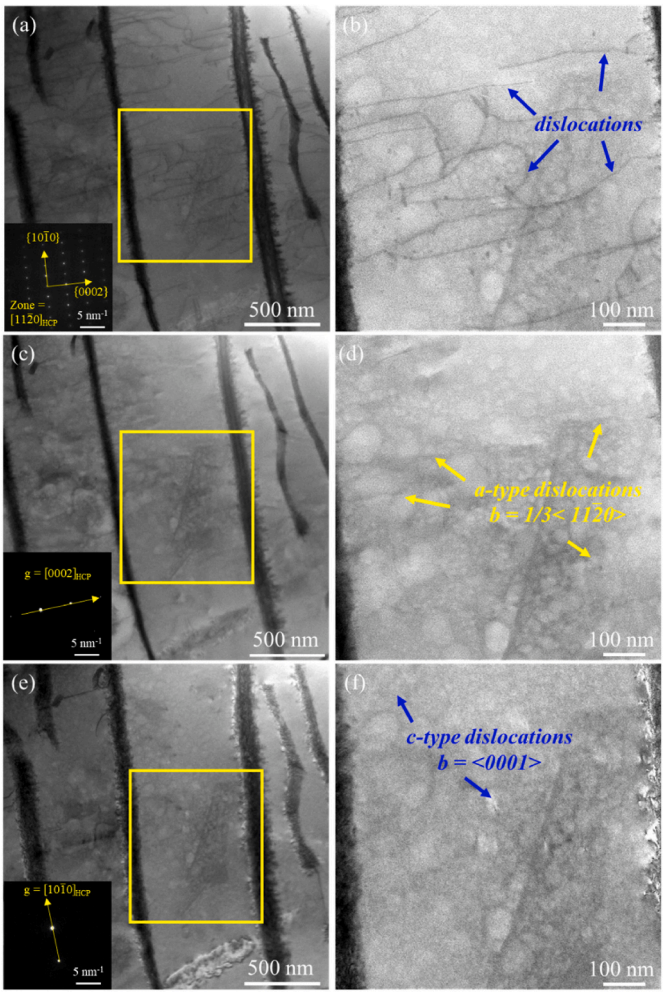

Fig. 11. (a) Bright-field TEM image of lamellar structure after tensile testing. (b) High-magnification TEM image showing dislocation distribution within a single α lamella. (c) Bright-field TEM image of β transformed structure and SAED pattern of {0002} orientation. (d) High-magnification TEM image showing dislocation distribution within a single α lamella under {0002} orientation. (e) Bright-field TEM image of the β transformed structure and SAED pattern of $\{10\bar{1}0\}$ orientation. (f) high-magnification TEM image showing dislocation distribution within a single α lamella under $\{10\bar{1}0\}$ orientation.

between localized stress concentration and deformation twins is the main driving mechanism for micro-void nucleation [45,46]. At moderate strain levels, these micro-voids undergo further growth and coalescence, ultimately leading to the formation of microcracks. As the strain increases, the micro-cracks exhibit continuous propagation preferentially along high strain gradients such as twin boundaries or adjacent slip bands, which usually act as favorable crack propagation path due to the enhanced local stress field [47].

Furthermore, deformation twinning-induced non-reversible lattice reorientation is a well-established source of cyclic tension-compression asymmetry in HCP materials [48,49]. This asymmetry often manifests as the evolution of mean stress/strain (ratcheting) under stress-controlled cyclic loading, which can significantly accelerate fatigue damage accumulation, lead to premature failure, and consequently reduce fatigue life [50,51]. Secondly, the formation of twin boundaries can markedly influence early crack initiation. These boundaries can act as effective barriers to slip, resulting in localized stress concentrations that promote crack nucleation [43,52]. Alternatively, the irreversible shear displacement associated with twinning can itself generate surface relief or intrusions/extrusions, which serve as preferential sites for crack initiation [48–50].

The aforementioned results clearly indicate that $\{10\bar{1}2\}\langle10\bar{1}1\rangle$ tensile twin is one of the primary plastic deformation mechanisms in Ti6321 alloy. This observed dominance of twinning under uniaxial tensile suggests a potential for pronounced tension-compression asymmetry and texture-induced ratcheting behavior under cyclic loading conditions, a phenomenon well-documented in other HCP materials with intense textures. For instance, the study by Gryguć et al. [48] demonstrated that in forged AZ80 magnesium alloy, the propensity for tensile twinning during the compression reversal leads to highly asymmetric hysteresis loops and the development of a significant compressive mean strain. Although the present study focuses on the uniaxial deformation of Ti6321 alloy, the clear relationship established here among microstructure, texture, and twin-dominated deformation provides a microstructural basis for predicting similar asymmetric cyclic responses in this Ti alloy and other HCP materials. This connection ultimately enhances the applicability of our findings for components subjected to cyclic service loads.

The mechanistic understanding established in this work points toward clear pathways for optimizing the Ti-6321 alloy. Future efforts will focus on tailoring its microstructure through thermo-mechanical processing to refine the grain size and control crystallographic texture, thereby suppressing deformation twinning and promoting more homogeneous slip [49–55].

5. Conclusions

In this study, in-situ EBSD observation of Ti−6321 alloy during uniaxial tensile deformation was employed to systematically elaborate the microstructure evolution, with particular emphasis on revealing the mechanisms of slip system activation and twinning deformation. The main findings are listed as follows.

(1) Prismatic and basal <a> slip systems dominate the deformation behavior at low strains, while pyramidal <a> and <c+a> slip systems become the predominant plastic deformation mechanisms under high strain conditions.
(2) During in-situ tensile testing, the equiaxed α phase preferentially activates basal slip as the primary deformation mechanism at low strain levels. In contrast, the β transformed structure predominantly initiates the prismatic slip systems to accommodate initial deformation. With increasing strain, the lamellar α phase within the β transformed structure activates the pyramidal <c+a> slip systems under the constraint effect of phase boundaries, and thereby the strain accommodation along the c-axis is facilitated.
(3) $\{10\bar{1}2\}\langle\bar{1}011\rangle$ tensile twinning induces lattice reorientation through shear deformation, and the initial c-axis orientation unfavorable for dislocation slip is gradually transformed into a more favorable configuration. This deformation mechanism effectively compensates for the insufficient slip systems in HCP structures, thereby providing a coordinated mechanism for accommodating c-axis strain.
(4) During in-situ tensile deformation, gliding dislocations are obstructed by the abrupt crystallographic orientation change at twin boundaries, leading to the formation of dislocation pile-up zones in the interfacial regions. This synergistic interaction between dislocation slips and twinning deformation governs the nucleation and propagation of micro-voids through local stress concentration mechanisms.

CRediT authorship contribution statement

Yafei Wang: Writing – original draft, Visualization, Validation, Resources, Project administration, Investigation, Data curation, Conceptualization. **Shuangjie Chu:** Visualization, Validation, Supervision, Resources, Project administration, Formal analysis, Conceptualization.

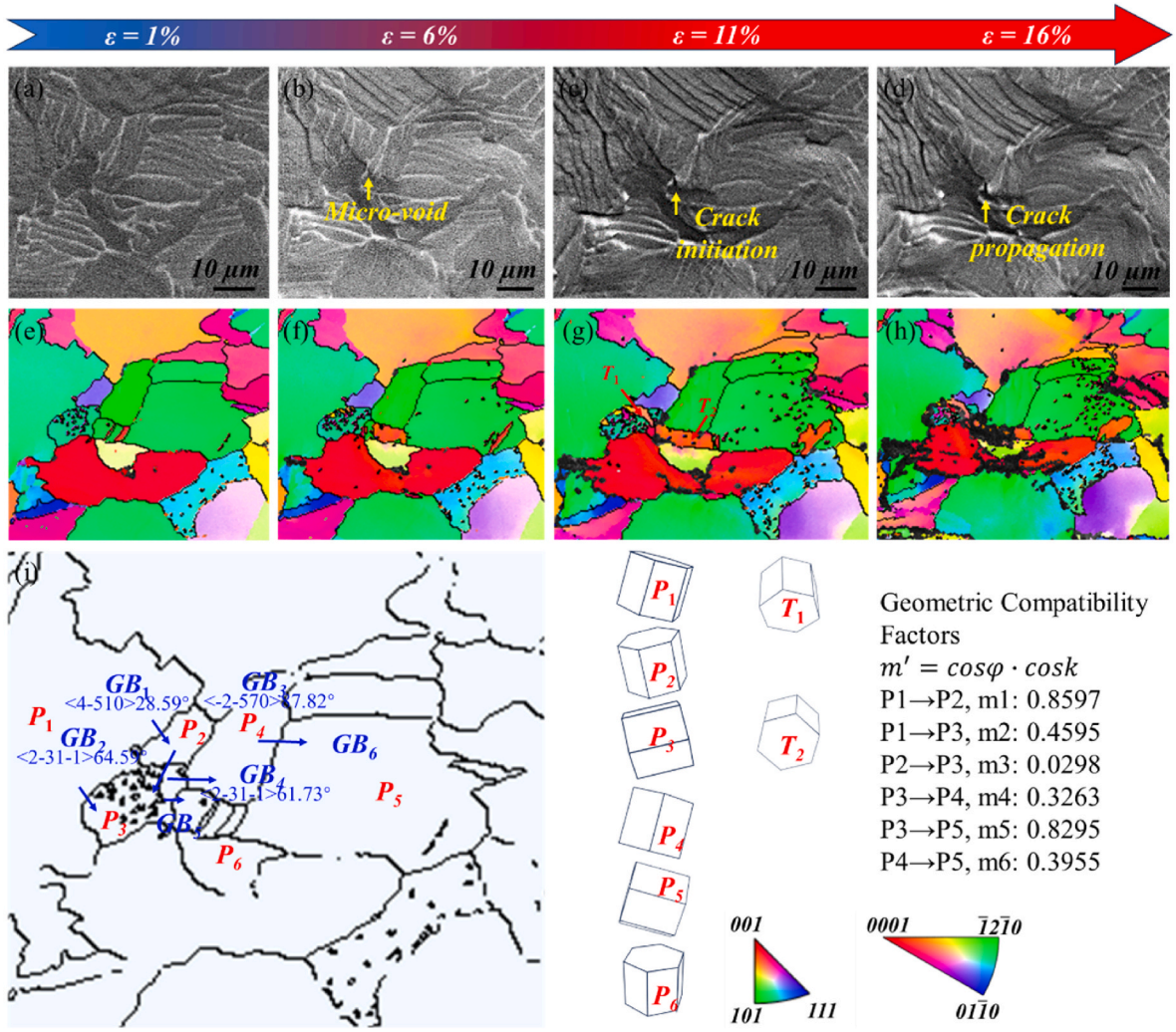

Fig. 12. SEM images (a–d) and IPF maps (e–h) at strain of (a, e) 1 %, (b, f) 6 %, (c, g) 11 % and (d, h) 16 % (The yellow circle indicates the initiation and propagation of the crack). (i) Grain boundary map showing the misorientation and rotation axis between several adjacent grains (T_1 and T_2 represent the tensile twins). (For interpretation of the references to colour in this figure legend, the reader is referred to the Web version of this article.)

Xing Zhang: Writing – review & editing, Methodology, Investigation, Data curation, Conceptualization. **Wanting Sun:** Writing – review & editing, Project administration, Methodology, Investigation. **Qifei Zhang:** Validation, Supervision, Formal analysis, Data curation. **Qian Liu:** Methodology, Investigation, Formal analysis. **Soban Muddassir Dar:** Resources, Methodology, Investigation, Formal analysis. **Bohao Zhou:** Resources, Methodology, Investigation, Formal analysis. **Jifeng Sun:** Methodology, Investigation, Data curation, Conceptualization. **Gaofei Liang:** Software, Resources, Project administration, Investigation. **Haiyan Zhao:** Resources, Formal analysis, Data curation, Conceptualization. **Bo Mao:** Writing – review & editing, Writing – original draft, Validation, Investigation, Funding acquisition, Formal analysis, Data curation, Conceptualization.

Declaration of competing interest

The authors declare that they have no known competing financial interests or personal relationships that could have appeared to influence the work reported in this paper.

Acknowledgements

The authors acknowledge with gratitude funding received from the National Key R&D Program of China (No. 2022YFB3705603), Scientific Research Plan Project of Shanghai, P.R. China (No. 22SQBS00600), the Excellent Youth Overseas Project of National Science and Natural Foundation of China, the National Natural Science Foundation of China (No. 52571089), and the Advanced Materials-National Science and Technology Major Project of China (No. 2025ZD0612000).

Appendix

Table 1S
The geometric compatibility factors for different slip systems from grain P1 and P2.

P1	P2		
	Basal slip $[2\bar{1}\bar{1}0]$ SF = 0.1443	Basal slip $[\bar{1}2\bar{1}0]$ SF = 0.0612	Basal slip $[\bar{1}\bar{1}20]$ SF = 0.2055
Basal slip $[2\bar{1}\bar{1}0]$ SF = 0.0581	0.4875	0.8207	0.3332
Basal slip $[\bar{1}2\bar{1}0]$ SF = 0.1678	0.8597	0.4298	0.4300
Basal slip $[\bar{1}\bar{1}20]$ SF = 0.2259	0.3722	0.3910	0.7632

Table 2S
The geometric compatibility factors for different slip systems from grain P1 and P3.

P1	P3		
	Basal slip $[2\bar{1}\bar{1}0]$ SF = 0.1938	Basal slip $[\bar{1}2\bar{1}0]$ SF = 0.0361	Basal slip $[\bar{1}\bar{1}20]$ SF = 0.2299
Basal slip $[2\bar{1}\bar{1}0]$ SF = 0.0581	0.2977	0.4595	0.1618
Basal slip $[\bar{1}2\bar{1}0]$ SF = 0.1678	0.0462	0.3509	0.3047
Basal slip $[\bar{1}\bar{1}20]$ SF = 0.2259	0.2514	0.1086	0.1429

Table 3S
The geometric compatibility factors for different slip systems from grain P2 and P3.

P2	P3		
	Basal slip $[2\bar{1}\bar{1}0]$ SF = 0.1938	Basal slip $[\bar{1}2\bar{1}0]$ SF = 0.0361	Basal slip $[\bar{1}\bar{1}20]$ SF = 0.2299
Basal slip $[2\bar{1}\bar{1}0]$ SF = 0.1443	0.0082	0.0249	0.0167
Basal slip $[\bar{1}2\bar{1}0]$ SF = 0.0612	0.0108	0.0298	0.0190
Basal slip $[\bar{1}\bar{1}20]$ SF = 0.2055	0.0026	0.0049	0.0023

Table 4S
The geometric compatibility factors for different slip systems from grain P3 and P4.

P4	P3		
	Basal slip $[2\bar{1}\bar{1}0]$ SF = 0.1938	Basal slip $[\bar{1}2\bar{1}0]$ SF = 0.0361	Basal slip $[\bar{1}\bar{1}20]$ SF = 0.2299
Basal slip $[2\bar{1}\bar{1}0]$ SF = 0.1965	0.3189	0.2040	0.1149
Basal slip $[\bar{1}2\bar{1}0]$ SF = 0.0062	0.3263	0.4634	0.1371
Basal slip $[\bar{1}\bar{1}20]$ SF = 0.2028	0.0073	0.2594	0.2521

Table 5S
The geometric compatibility factors for different slip systems from grain P3 and P5.

P5	P3		
	Basal slip $[2\bar{1}\bar{1}0]$ SF = 0.1938	Basal slip $[\bar{1}2\bar{1}0]$ SF = 0.0361	Basal slip $[\bar{1}\bar{1}20]$ SF = 0.2299
Basal slip $[2\bar{1}\bar{1}0]$ SF = 0.0678	0.6275	0.8295	0.2020
Basal slip $[\bar{1}2\bar{1}0]$ SF = 0.1709	0.1116	0.6404	0.7520

(*continued on next page*)

Table 5S (*continued*)

P5	P3		
	Basal slip $[2\bar{1}\bar{1}0]$ SF = 0.1938	Basal slip $[\bar{1}2\bar{1}0]$ SF = 0.0361	Basal slip $[\bar{1}\bar{1}20]$ SF = 0.2299
Basal slip $[\bar{1}\bar{1}20]$ SF = 0.2386	0.7391	0.1891	0.5500

Table 6S
The geometric compatibility factors for different slip systems from grain P4 and P5.

P5	P4		
	Basal slip $[2\bar{1}\bar{1}0]$ SF = 0.1965	Basal slip $[\bar{1}2\bar{1}0]$ SF = 0.0062	Basal slip $[\bar{1}\bar{1}20]$ SF = 0.2028
Basal slip $[2\bar{1}\bar{1}0]$ SF = 0.0678	0.3344	0.3525	0.0180
Basal slip $[\bar{1}2\bar{1}0]$ SF = 0.1709	0.1899	0.3955	0.2057
Basal slip $[\bar{1}\bar{1}20]$ SF = 0.2386	0.1446	0.0431	0.1876

Appendix A. Supplementary data

Supplementary data to this article can be found online at https://doi.org/10.1016/j.msea.2025.149705.

Data availability

Data will be made available on request.

References

[1] Q. Tang, P. Qi, T. Wang, J. Hu, J. Yin, B. Li, Z. Nie, Formation mechanism of lamellar bimodal microstructure and mechanical property in the high temperature near α titanium alloy, J. Alloys Compd. 938 (2023).
[2] F. Hao, X. Liu, Y. Du, Y. Mao, H. Chen, S. Li, K. Wang, L. Lei, Excellent dynamic mechanical properties of a newly developed titanium alloy with bimodal structure, J. Alloys Compd. 961 (2023).
[3] D. Zhou, W. Zeng, J. Xu, S. Wang, W. Chen, Evolution of equiaxed and lamellar α during hot compression in a near alpha titanium alloy with bimodal microstructure, Mater. Char. 151 (2019) 103–111.
[4] B. Sun, X. Huang, Y. Pan, T. Yan, Y. Zhang, M. Sun, Z. Liu, L. Fan, X. Li, A comparative study on the passive film and SCC behavior of Ti-6Al-3Nb-2Zr-1Mo alloy at various test temperatures in simulated seawater, Corros. Sci. 233 (2024).
[5] H. Wu, L. Wang, Y. Wang, H. Tian, Y. Xin, J. Hou, Z. Cui, Comparative study of the corrosion behavior of base metal and welded joint of Ti-6Al-3Nb-2Zr-1Mo alloy in the acidic chloride environment, Corros. Sci. 244 (2025).
[6] T. Chen, Z. Zeng, H. Gao, C. Liu, Z. Liu, Z. Sun, X. Li, Influence of AC/DC on stress corrosion cracking of Ti-6Al-3Nb-2Zr-1Mo alloy in simulated marine solution, Int. J. Hydrogen Energy 55 (2024) 177–188.
[7] X. Chen, L. Zhang, Y. Xiong, H. Yao, F. Ren, J. Zhang, Effects of supersonic fine particle bombardment on the microstructure and corrosion properties of Ti-6Al-3Nb-2Zr-1Mo alloy, Surf. Coat. Technol. 459 (2023).
[8] G. Luo, L. Zhang, Y. Xiong, B. Zhang, X. Chen, Y. Wu, S. Wang, W. Cao, Effect of laser shock peening on the corrosion properties of Ti-6Al-3Nb-2Zr-1Mo alloy, Surf. Coat. Technol. 440 (2022).
[9] S. Xu, H. Zhang, N. Xiao, R. Qiu, Z. Cui, M. Fu, Mechanisms of macrozone elimination and grain refinement of near α Ti alloy via the spheroidization of the Widmannstätten structure, Acta Mater. 260 (2023) 119339.
[10] C. Tan, Q. Sun, L. Xiao, Y. Zhao, J. Sun, Characterization of deformation in primary α phase and crack initiation and propagation of TC21 alloy using in-situ SEM experiments, Mater. Sci. Eng., A 725 (2018) 33–42.
[11] H. Shao, Y. Zhao, P. Ge, W. Zeng, In-situ SEM observations of tensile deformation of the lamellar microstructure in TC21 titanium alloy, Mater. Sci. Eng., A 559 (2013) 515–519.
[12] R. Jia, W. Zeng, Z. Zhao, P. Zhang, J. Xu, Q. Wang, In-situ investigation on the deformation mechanism of duplex microstructure of a near α titanium alloy, J. Alloys Compd. 893 (2022).
[13] W. Li, S. Yamasaki, M. Mitsuhara, H. Nakashima, In situ EBSD study of deformation behavior of primary α phase in a bimodal Ti-6Al-4V alloy during uniaxial tensile tests, Mater. Char. 163 (2020) 110282.
[14] L. Wang, X. Fan, J. Yu, F. Lu, M. Zhan, Q. Chen, Insight into the multi-hierarchical interactions between α and β phases during hot deformation of near-β titanium alloy, Mater. Sci. Eng., A 903 (2024) 146649.
[15] Baoxian Su, Liangshun Luo, Binbin Wang, Yanqing Su, Liang Wang, Robert O. Ritchie, Enyu Guo, Ting Li, Huimin Yang, Haiguang Huang, Jingjie Guo, H. Fu, Annealed microstructure dependent corrosion behavior of Ti-6Al-3Nb-2Zr-1Mo alloy, J. Mater. Sci. Technol. 62 (2021) 234–248.
[16] K. Meng, K. Guo, Q. Yu, D. Miao, C. Yao, Q. Wang, T. Wang, Effect of annealing temperature on the microstructure and corrosion behavior of Ti-6Al-3Nb-2Zr-1Mo alloy in hydrochloric acid solution, Corros. Sci. 183 (2021).
[17] W.Y. Guo, J. Sun, J.S. Wu, Electrochemical and XPS studies of corrosion behavior of Ti–23Nb–0.7Ta–2Zr–O alloy in Ringer's solution, Mater. Chem. Phys. 113 (2–3) (2009) 816–820.
[18] L. Meng, T. Kitashima, P. Lin, L. Zheng, Z. Jiang, J. Zhao, In situ EBSD investigation of microtexture evolution and slip activation of α macrozones during tensile deformation in Ti-6Al-4V alloy, Mater. Sci. Eng., A 924 (2025).
[19] W. Macek, R. Branco, J. de Jesus, J.D. Costa, S.-P. Zhu, R. Masoudi Nejad, A. Gryguć, Strain energy density and entire fracture surface parameters relationship for LCF life prediction of additively manufactured 18Ni300 steel, Int. J. Damage Mech. 33 (9) (2024) 725–747.
[20] S. Wei, K.S. Kim, J. Foltz, C.C. Tasan, Discovering pyramidal treasures: multi-scale design of high strength–ductility titanium alloys, Adv. Mater. 36 (33) (2024).
[21] C. Tan, Q. Sun, L. Xiao, Y. Zhao, J. Sun, Slip transmission behavior across α/β interface and strength prediction with a modified rule of mixtures in TC21 titanium alloy, J. Alloys Compd. 724 (2017) 112–120.
[22] F. Bridier, P. Villechaise, J. Mendez, Analysis of the different slip systems activated by tension in a α/β titanium alloy in relation with local crystallographic orientation, Acta Mater. 53 (3) (2005) 555–567.
[23] J. Zhao, L. Lv, K. Wang, G. Liu, Effects of strain state and slip mode on the texture evolution of a near-α TA15 titanium alloy during hot deformation based on crystal plasticity method, J. Mater. Sci. Technol. 38 (2020) 125–134.
[24] J. Tian, J.-f. Deng, Y. Chang, Y. Zhou, W. Liang, J. Ma, Selection behavior of {10−12} tensile twin variants and its contribution during plastic processing of magnesium alloy, J. Alloys Compd. 918 (2022).
[25] M. Arul Kumar, B. Clausen, L. Capolungo, R.J. McCabe, W. Liu, J.Z. Tischler, C. N. Tomé, Deformation twinning and grain partitioning in a hexagonal close-packed magnesium alloy, Nat. Commun. 9 (1) (2018).
[26] J. Hui, X. Zhang, T. Liu, W. Liu, B. Wang, First-principles calculation of twin boundary energy and strength/embrittlement in hexagonal close-packed titanium, Mater. Des. 213 (2022).
[27] L. Zhang, H. Xin, D. Zhao, Z. Li, S. Ma, Effect of twin boundary density on mechanical behavior of Al0.1CoCrFeNi high-entropy alloy by molecular dynamics simulation, Front. Mater. 9 (2022).
[28] J.-f. Deng, J. Tian, Y. Chang, Y. Zhou, W. Liang, J. Ma, The role of {10–12} tensile twinning in plastic deformation and fracture prevention of magnesium alloys, Mater. Sci. Eng., A 853 (2022).
[29] K. Wei, R. Hu, D. Yin, L. Xiao, S. Pang, Y. Cao, H. Zhou, Y. Zhao, Y. Zhu, Grain size effect on tensile properties and slip systems of pure magnesium, Acta Mater. 206 (2021).
[30] G. Meric de Bellefon, J.C. van Duysen, Tailoring plasticity of austenitic stainless steels for nuclear applications: review of mechanisms controlling plasticity of austenitic steels below 400 °C, J. Nucl. Mater. 475 (2016) 168–191.
[31] B. Ju, X. Liu, J. Zhou, J. Lei, Y. Du, N. Zhao, Z. Zheng, K. Li, D. Zhao, W. Chen, Temperature-dependent tensile behaviors and strain localization of TC17 high

temperature titanium alloys with bimodal microstructure, Mater. Char. 223 (2025).
[32] S.N. Monteiro, L.P. Brandão, T.G.d. Sousa, F.d.C. Garcia Filho, Novel methods for dislocation density estimation in highly compacted tangles, J. Mater. Res. Technol. 9 (2) (2020) 2072–2078.
[33] S. Yefimov, E. Van der Giessen, Multiple slip in a strain-gradient plasticity model motivated by a statistical-mechanics description of dislocations, Int. J. Solid Struct. 42 (11–12) (2005) 3375–3394.
[34] Y. Ru, S. Li, J. Zhou, Y. Pei, H. Wang, S. Gong, H. Xu, Dislocation network with pair-coupling structure in {111} γ/γ′ interface of Ni-based single crystal superalloy, Sci. Rep. 6 (1) (2016).
[35] B.A.S.B.C. Ng, M.A. Crimp, T.R. Bieler, The role of mechanical twinning on microcrack nucleation and crack propagation in a near-γ TiAl alloy, Intermetallics 12 (2004) 1317–1323.
[36] R. Zhang, Q. Zhao, D. Guo, Y. Mao, Z. Qiao, Y. Zhao, Multiscale analysis of synergistic interactions of twins and multiple factors inducing high cryogenic impact toughness in CT20 alloy, J. Mater. Sci. Technol. 236 (2025) 225–244.
[37] S. Diiorio, L. Briottet, E. Rauch, D. Guichard, Plastic deformation, damage and rupture of PM Ti–6Al–4V at 20K under monotonic loading, Acta Mater. 55 (1) (2007) 105–118.
[38] X. Zhang, F.P.E. Dunne, Short crack propagation near coherent twin boundaries in nickel-based superalloy, Int. J. Fatig. 172 (2023) 107586.
[39] J. Shen, H. Fan, J. Wang, G. Zhang, R. Pan, Z. Huang, Stored energy density research on the fatigue crack initiation at twin boundary and life prediction of Inconel718 superalloy, Int. J. Fatig. 171 (2023) 107590.
[40] R. Xin, Y. Liang, C. Ding, C. Guo, B. Wang, Q. Liu, Geometrical compatibility factor analysis of paired extension twins in extruded Mg–3Al–1Zn alloys, Mater. Des. 86 (2015) 656–663.
[41] M.M.J. Luster, Compatibility of deformation in two-phase Ti-Al alloys Dependence on microstructure and orientation relationships, Metall. Mater. Trans. 26 (7) (1995) 1745–1756.
[42] X. Han, K. Li, Y. Deng, M. Zhang, J. Li, Research on the effect of micro-voids on the deformation behavior and crack initiation lifetime of titanium alloy under cyclic loading by crystal plasticity finite element method, J. Mater. Res. Technol. 22 (2023) 3218–3229.
[43] L.W. Bijin Zhou, Peipeng Jin, Hailong Jia, Hans Jørgen Roven, Xiaoqin Zeng, Yanjun Li, Revealing slip-induced extension twinning behaviors dominated by micro deformation in a magnesium alloy, Int. J. Plast. 128 (2020) 102669.
[44] M.R.M. Lentz, N. Schaefer, W. Reimers, I.J. Beyerlein, Strength and ductility with $\{10\bar{1}1\}$ — $\{10\bar{1}2\}$ double twinning in a magnesium alloy, Nat. Commun. 7 (11068) (2016) 11068.
[45] M. Bönisch, Y. Wu, H. Sehitoglu, Hardening by slip-twin and twin-twin interactions in FeMnNiCoCr, Acta Mater. 153 (2018) 391–403.
[46] M.D. Sangid, T. Ezaz, H. Sehitoglu, Energetics of residual dislocations associated with slip–twin and slip–GBs interactions, Mater. Sci. Eng., A 542 (2012) 21–30.
[47] Z.W. Huang, P.L. Yong, N.N. Liang, Y.S. Li, Slip, twinning and twin-twin interaction in a gradient structured titanium, Mater. Char. 149 (2019) 52–62.
[48] A. Gryguc, S.B. Behravesh, S.K. Shaha, H. Jahed, M. Wells, B. Williams, X. Su, Low-cycle fatigue characterization and texture induced ratcheting behaviour of forged AZ80 Mg alloys, Int. J. Fatig. 116 (2018) 429–438.
[49] A. Gryguć, S.B. Behravesh, S.K. Shaha, H. Jahed, M. Wells, B. Williams, X. Su, Multiaxial cyclic behaviour of extruded and forged AZ80 Mg alloy, Int. J. Fatig. 127 (2019) 324–337.
[50] Q. Yu, J. Zhang, Y. Jiang, Q. Li, Multiaxial fatigue of extruded AZ61A magnesium alloy, Int. J. Fatig. 33 (3) (2011) 437–447.
[51] C. Liu, R. Thomas, T. Sun, J. Donoghue, X. Zhang, T.L. Burnett, J.Q. da Fonseca, M. Preuss, Multi-dimensional study of the effect of early slip activity on fatigue crack initiation in a near-α titanium alloy, Acta Mater. 233 (2022).
[52] P. Yang, Q. Sun, X. Zheng, X. Mi, L. Chai, M. Zhu, Revealing the correlation between microstructure and fatigue crack growth behaviors in Ti–6Al–3Nb–2Zr–1Mo alloy, Mater. Sci. Eng., A 848 (2022).
[53] H.L. Bingshu Wang, Yonggan Zhang, Baoxue Zhou, Liping Deng, Chen Wang, Junfeng Chen, Yonghao Zhang Effect of grain size on twinning behavior of pure titanium at room temperature, Mater. Sci. Eng., A 827 (2021) 142060.
[54] M.A. Kumar, I.J. Beyerlein, Influence of plastic properties on the grain size effect on twinning in Ti and Mg, Mater. Sci. Eng., A 771 (2020).
[55] Q. Yu, Z.-W. Shan, J. Li, X. Huang, L. Xiao, J. Sun, E. Ma, Strong crystal size effect on deformation twinning, Nature 463 (7279) (2010) 335–338.